

A pedophysical relationship between X-ray Computed Tomography and Electrical Resistivity data

Mihai O. Cimpoişu^{1,2}, Oliver Kuras², Tony Pridmore³ and Sacha J. Mooney¹

¹Division of Agriculture and Environmental Science, School of Bioscience,
University of Nottingham, Sutton Bonington, Leicestershire, LE12 5RD, UK
E-mail: mcim@bgs.ac.uk

²Geophysical Tomography Team, British Geological Survey,
Keyworth, Nottinghamshire, NG12 5GG, UK

³School of Computer Science, University of Nottingham, Wollaton Road,
Nottingham, Nottinghamshire, NG8 1BB, UK

ABSTRACT

Quantitatively linking observations from independent non-invasive soil assessment methods enhances our ability to understand root zone processes. Electrical Resistivity Tomography (ERT) and X-ray Computed Tomography (CT) are two advanced non-invasive technologies routinely employed in soil science. ERT allows 4D process monitoring (e.g. solute transport) and is sensitive to changes in moisture content (MC) and soil texture. X-ray CT is a higher resolution method used to appraise soil structure. We measured the variation of electrical resistivity and X-ray absorption with gravimetric moisture content (GMC) for two distinct soil types. Experimental results were compared with existing pedophysical relationships that express these dependencies. Based on the good fit between measurements and model predictions, we formulated a new pedophysical relationship that links directly the two soil properties. This will allow a direct translation between ERT and X-ray data for the study of root-zone parameters under well-defined experimental circumstances.

Introduction

A very important aspect of root zone processes is understanding the behaviour of water in soils. Consequently, linking soil hydraulic properties, such as water retention curve and hydraulic conductivity, with soil structure is essential for understanding processes that control soil functions (van Genuchten and Pachepsky, 2011), such as water storage or food production.

In recent years, the scientific community has sought to develop numerous non-invasive methods that preserve soil structural integrity. We can distinguish two categories of methods: static, offering higher spatial resolution, such as Neutron Radiography (Shokri et al., 2008) or X-ray CT (Tracy et al., 2015) and dynamic ones offering higher temporal resolution, such as Electrical Resistivity Tomography (Cassiani et al., 2016) or Time-Domain Reflectometry (Nyberg, 1996). The methods in the latter category enable time-lapse monitoring and give greater flexibility, as they can be employed both in the lab (Garre' et al., 2011) and in the field (Boaga et al., 2013). Instead, the static methods attain greater spatial resolution (pore-scale - μm – mm) and a very high contrast sensitivity between different soil matrix components, such as minerals, water, air-filled pore space (Wildenschild et al., 2002).

Past research suggests a strong correlation between visually derived soil structural information and other soil intrinsic properties. Mueller et al. (2009) showed that physical properties and qualities, such as dry bulk density or soil strength, correlate significantly with visually observed structure, such as aggregate shape and size. Paradelo et al. (2016) correlated CT-derived parameters with water transport in soils and suggested the potential of the method to estimate air, water and solutes fluxes at the field scale.

Lewis and Sjoström (2010) emphasized the importance of having appropriate pedophysical

47 calibrations for a fluid infiltration experiment on a soil monolith. For ERT monitoring experiments, prior
48 calibration is needed in order to translate electrical resistivity (ER) into values of MC. Such calibrations
49 can be done by regression analysis comparing resistivity results with MC measurements made
50 independently (Srayeddin and Doussan, 2009) or by using a pedophys- ical relationship (Beff et al., 2013).

51 In this study we focus on two methods: ERT has been frequently employed for monitoring water
52 content in the root zone (Samouëlian et al., 2005), whilst X-ray CT has proven to be very successful for
53 assessing soil structure (Peyton et al., 1992) and reconstructing root architecture (Mooney et al., 2012).
54 We establish a quantitative link between X-ray absorption, the parameter representative for the structural
55 information contained in the CT scans, and bulk resistivity, which is an electrical property of soils and the
56 measurable parameter for ERT. In order to test the validity of our methodology for different soil textures
57 we sampled two soil types, clay loam and silt clay loam. Subsequently, we measured the ER and average
58 X-ray absorption of both soils as a function of MC. By fitting known pedophysical models, which express
59 the dependence of either physical parameters on MC, to the laboratory measurements, we obtain soil-
60 specific calibration curves corresponding to the two different textures. Encouraged by the good fit
61 between measurements and models we derive a quantitative link between x-ray absorption and ER of the
62 soil by rearranging the pedophysical expressions. Finally, we propose an alternative strategy for the
63 quantitative interpretation of electrical measurements based on water content estimates obtained from X-
64 ray CT scans.

65 Theoretical background

66 Basic principles of ERT and X-ray CT

67 X-ray CT allows visualization of the interior structure of a target object due to the attenuation
68 properties of electro- magnetic waves. X-rays are produced in a tube containing an anode and a cathode
69 when a voltage is applied across the electrodes. The Beer-Lambert equation describes the X-ray beam
70 attenuation as it passes through a target medium (Wildenschild et al., 2002):

$$71 \quad I = I_0 \exp(-\mu * D), \quad (1)$$

72 where D is the thickness, μ is the attenuation coefficient, and I_0 and I are the intensities before and after passing
73 through the sample. In medical CT scanners the source-detector pair rotates whereas in industrial scanners the
74 source-detector pair is fixed and the sample rotates, allowing projections from different angles. From these
75 measurements, 3D structures can be digitally reconstructed as volumes of pixels expressed in grayscale (GS)
76 values, which represent the X-ray attenuation coefficient of the volume element.

77 ERT is a near-surface geophysical method that uses electrical resistance measurements in order to
78 reconstruct an image of the bulk electrical resistivity of the subsurface. Small electrical currents are
79 injected into the ground and the resulting electrical potential difference is recorded. Resistivity (or its
80 inverse conductivity - σ) is obtained using Ohm's law:

$$81 \quad \rho = K * \frac{\delta V^*}{I}, \quad (2)$$

82 where I is the injected current, δV is the electrical potential difference and K is the formation factor which
83 depends on the geometric arrangement of electrodes.

84 Known pedophysical models

85 Archie (1942) formulated one of the first petrophysical relationships to describe the dependency
86 of ER on MC in porous rocks. Building on Archie's relation, the Waxman Smits (WS) model includes
87 surface conductivity effects, which become important when an increased content of clay particles is
88 present (Waxman and Smits, 1968).

89 In this study we used a modified formulation of WS (Chambers et al., 2014):

$$\rho(GMC) = F * \frac{(1-\Phi)*D_g*GMC^{-n}}{\Phi*D_w} * \left(\sigma_w + B_{ws} * \frac{(1-\Phi)*D_g*c}{100\Phi} * \frac{\Phi*D_w}{(1-\Phi)*D_g*GMC} \right)^{-1}, \quad (3)$$

where $F = \Phi^{-m}$ is the formation factor, Φ is porosity, c is the cation exchange capacity, B_{ws} is the average ion mobility, σ_w is the water conductivity, D_g, D_w are the grain and water densities. In this model, m and n are empirical parameters. As its application has extended to soil studies we will refer to it here as a pedophysical relationship.

As described by Bailly et al. (2003), Beer-Lambert's law can be used to describe the contribution of various parameters to the overall absorption process. Baker et al. (2007) used this to formulate GMC in terms of dry and wet conditions:

$$GMC = \frac{\ln\left(\frac{I_{dry}}{I_{wet}}\right)}{\mu_{water} * x_{dry} * \rho_{dry}}, \quad (4)$$

where μ_{water} is water attenuation coefficient, x_{dry} is the dry thickness, ρ_{dry} is the dry density and I_{dry}, I_{wet} are the dry and wet X-ray intensities respectively. For simplicity, we will further refer to Equations (3) and (4) as BR and XA relationships respectively.

Methodology

A range of steps were undertaken to prepare the soil samples for X-ray CT and resistivity measurements. Following the acquisition of both datasets, we discuss data processing and the formulation of a combined pedophysical relationship. We also suggest an alternative method of obtaining a BR calibration based on CT estimates.

Soil sample preparation

Two soil types: clay loam (Clay:Silt:Sand (%) 65:23:12) - soil type 1 (S1) and silty clay loam (Clay:Silt:Sand (%) 52:39:9) - soil type 2 (S2), were sampled from University of Nottingham's Bunny Farm, Nottinghamshire, UK (Fieldsite 1: N 52.85593 W -1.12520 and Fieldsite 2: N 52.85743 W - 1.12723). In the subsequent discussion measurement set 1 corresponds to S1 and measurement set 2 to S2.

The samples were fragmented and sieved to < 5 mm aggregates. Afterwards, we dried them for 72 hours at 35°C, a temperature low enough to avoid the destruction of clay particles. The whole soil mass was then split into seven batches of three samples each for S1 and eight batches of three samples each for S2. To each batch we added different amounts of water by uniformly spraying the soil aggregates. Water addition was quantified by weighing the soil (GMC values in Fig.2 XA and BR). Finally, the soil was compacted into rectangular plastic receptacles (dimensions 2.5x2.5x7 cm).

Electrical and CT measurements

To facilitate resistivity measurements, stainless steel plate electrodes were placed at either end of each receptacle and two thin steel rod electrodes were inserted into the middle section. The electrode positioning resembles a Wenner geometry (Burger et al., 2006). The sample was left for 24 hours for moisture redistribution and equilibration. Afterwards, electrical resistance measurements were made with a Terrameter 4000 device, and using Equation (2) we estimated the ER of the samples.

To facilitate CT scanning, the electrodes were removed with minimal soil disruption. On the following day the samples were transported to the University of Nottingham's Hounsfield Facility where they were scanned with a v—Tome—x M X-ray scanner (Scan settings: 140 kV, 160 μ A, 8 minutes scan time and 30 μ m resolution).

Cross-sectional scan images were reconstructed using Volume Graphics 2.1 software over an 8 bit value range, implying each of the pixels had Gray Scale (GS) values in the interval 0(Black) - 255(White).

130 CT image processing

131 Each sample was reconstructed lengthwise and widthwise as two sets of 1400 and 500 cross-
132 sectional 'slice' images respectively (Fig. 1 I). From the whole image, a representative area was selected,
133 which was kept constant in every cross-sectional image. The selection, visualized in Fig. 1 II, does not
134 take into account the edges of the soil volume, which are more likely to have been subjected to
135 interactions with the exterior medium.

136 For every image, over the indicated area, an average GS value was computed, without taking into
137 account the pixels with very low (< 10 GS corresponding to air filled pore/fissure space) or very high (> 100
138 corresponding to high density minerals) GS values present in the sample, as we are strictly interested in the
139 soil material response to variations in MC. For both orientations, a GS value distribution along the sample
140 was computed from which the average and standard deviation have been derived.

141 Formulating a pedophysical link

142 Given the BR and XA relationships, we can compute an expression of ER as a function of X-ray
143 absorption by rear-ranging the two equations. Hence, we find:

$$144 \rho^{-1} = \frac{\ln \frac{I_{dry}}{I_{wet}}}{\rho_{dry} * x_{dry} * \mu_{water}}^{n-1} * \left(\frac{\ln \frac{I_{dry}}{I_{wet}}}{\rho_{dry} * x_{dry} * \mu_{water}} * \frac{\sigma_w}{\phi^{-m}} + B_{ws} * D_g * \frac{(1-\phi)*c}{\phi^{-m+1}} \right), \quad (5)$$

145 Except for m and n , all other soil and fluid properties in the combined expression above have been
146 measured independently in the laboratory (Table 1).

147 Enhancing BR predictions based on CT estimates

148 As described previously, calibration curves for interpreting ERT monitoring experiments are
149 obtained by taking bulk electrical resistivity measurements on samples of a known MC, estimated by
150 weighing. The water is added manually and its distribution is assumed to be uniform, therefore the
151 estimates are subject to error. An alternative option arises from the methodology described above. We
152 estimated the soil MC by fitting the XA model to our average GS measurements. These values were in
153 turn used to estimate ER on the basis of a BR relationship (Fig. 2 BR).

154 **Results and Discussion**

155 MC variability

156 Visual inspection of the image selections in Fig. 1 II, show how GS decreases with increasing MC. This
157 is also later confirmed by the average GS per sample estimates (Fig. 2 XA).
158 Fig. 2 shows a significant variance within the triplicate samples of the same batch. In order to determine the
159 source of this variance we have derived an average percentage of air-filled pores from the CT scans. It is
160 important to note that these estimates were recorded after the samples were packed so they will differ from
161 the soil's undisturbed values of air-filled porosity. For S1 we recorded values between 9.3 and 0.8 % with
162 larger air-filled porosity values corresponding to the first three batches with lower MC. In consequence, they
163 had the highest variance within the batch between the three replicates. For S2 we recorded a similar range of
164 values between 12.7 and 2.88 %. As for S1, the highest values and variance were observed within the first
165 three batches.

166 For S1 we noticed greater variation within the batches corresponding to the upper half of the
167 GMC distribution. This implies that when more moisture is present in the system the variations in GS are
168 higher. This can be explained by the way water redistributes once it enters the soil matrix. Capillary
169 pressure and movement of free water determine different regions of higher and lower MC Free (1911).
170 Therefore, an increased capillary activity may cause such variability. The percentage of air-filled pores
171 per sample batches showed a higher variance corresponding to the driest three batches for both soil types.
172 This implies a GMC threshold between 0.128 g. g^{-1} and 0.15 g. g^{-1} , over which, for this particular

173 sample size and geometry, a higher percentage of water-filled pores reduces the heterogeneity of water
174 distribution.

175 Implications of the pedophysical fit

176 For both soil types the conceptual models show a good fit with measured datasets (Fig. 2 XA and
177 BR and Table 1), implying the experimental data validates the model predictions. However, it is useful to
178 remember the pedophysical relations are case specific and correspond only to samples with the intrinsic
179 physical properties listed in this study (Table 1). Therefore, soil texture is an essential variable, which we
180 can also understand by observing the different shapes of the BR curves corresponding to the two soil
181 types.

182 For the BR model, the S1 exhibited higher resistivity values than S2 for low and medium GMC
183 (Fig. 2 BR). This effect may well be due to the difference in sample air-filled pore space, as an increase
184 implies an increase in electrical resistivity. However, our measurements do not support such statement as
185 the average percentage of air-filled pores is similar between the soil types. In the high GMC region,
186 where the majority of the pore-space has been occupied with water, the models produce similar values,
187 hence air-filled pore-space contribution to bulk values of resistance decreased. The electrical response is
188 also correlated with the soil clay content as it is directly linked to an electric charge deficit (Waxman and
189 Smits, 1968). Calculated cation exchange capacity (Table 1) supports the difference between S1 and S2
190 implying a clay content effect on resistance values recorded.

191 From the XA model we observe a more abrupt change in X-ray attenuation on the curve
192 corresponding to S1 (Fig. 2 XA). Also, S1 exhibits a higher dry GS value (intercept). Given the same X-
193 ray energy, the differences in absorption magnitude are also correlated to the sample's porosity and
194 texture. With increasing MC, a higher porosity implies a lower rate of saturation hence a higher
195 absorption increase rate.

196 Improving BR calibration

197 We proposed an alternative way of estimating water content for ERT experiment calibrations. In
198 Fig. 2 (BR) and Table 1 (BR lab and CT fit), the new estimates represent BR values based on CT
199 estimates of MC. These show a better fit with resistivity lab measurements than BR values (Model) based
200 on MC weighing for both soil types. We can also observe the new estimates correct the resistivity
201 underestimation for S1 in the high GMC region, but on the other hand underestimate the measured
202 resistivity values in the low GMC region. The conventional methodology is very laborious and time-
203 consuming with daily additions of extra water to subject samples which have to reach hydraulic
204 equilibrium before electrical measurements. The CT strategy we suggest allows simultaneous preparation
205 of multiple samples. Therefore, total experimental time is reduced to a few hours. Also, MC is derived for
206 each individual sample and not for each individual batch. We can state that from a theoretical point of
207 view, a calibration based on CT measurements is more advantageous and improves the calibration
208 estimates. However, we acknowledge that the use of X-ray CT is not always cost effective.

209 CT-ER relationship

210 In Equation (5) we formulated an expression for bulk ER as a function of X-ray intensity. As
211 seen in Fig. 2 Combined and based on the Pearson r and RMSError values (Table 1) the model fits well the
212 corresponding datasets. We observed an underestimation of electrical resistance in the low GS region of
213 the S1, which was a consequence of BR inaccuracy. For S2 we did not observe this behaviour, but BR
214 also accurately predicted the resistivity in the high GMC region. We extended the models beyond the
215 dataset boundaries and towards both ends the estimations asymptotically tend to a constant. For low values
216 of GS the value implies reaching soil water saturation and for the high values implies reaching a dry state,
217 zero GMC.

Conclusion

We have presented a methodology that facilitates the joint appraisal of datasets obtained through two well established non-invasive soil observation methods: X-ray CT and ERT. We obtained laboratory measurements of resistivity and average X-ray absorption for two soil types at different GMC. Subsequently, we fitted our results to representative MC pedophysical relations - Equations (3) and (4). The good fit between the model and measured datasets enabled us to: 1. rearrange the pedophysical equations in order to formulate a quantitative link between CT images and ER and 2. obtain an improved BR soil resistivity calibration based on X-ray CT estimates of MC. These results indicate the possibility of inferring electrical properties from CT images of soil and can be used as a benchmark calibration reference for future joint studies which employ the two methods. Further research should use such a relationship for a more comprehensive investigation of soil hydraulic properties by directly correlating MC distribution due to soil structure to changes in electrical resistance due to water infiltration flux or evapotranspiration. Furthermore, these new insights allow the development of improved geoelectrical calibrations that will enhance the ability to non-invasively monitor vadose zone processes, vital for agriculture management or civil engineering.

References

- Archie, G. (1942). The Electrical Resistivity Log as an Aid in Determining Some Reservoir Characteristics. *Transactions of the AIME*, **146**:54—62.
- Bailly, D., Campbell, M., Poffa, N., Sun, J., Galbraith, G., Mclean, R., Sanders, C., and Nelsen, G. (September 2003). Moisture transport studies in building materials. *Proceedings of Institute of Physics Conference: Sensors and their Applications XII*, pages 551—557.
- Baker, P. H., Bailly, D., Campbell, M., Galbraith, G. H., McLean, R. C., Poffa, N., and Sanders, C. H. (2007). The application of X-ray absorption to building moisture transport studies. *Measurement: Journal of the International Measurement Confederation*, **40**(9-10):951—959.
- Beff, L., Günther, T., Vandoorne, B., Couvreur, V., and Javaux, M. (2013) Three-dimensional monitoring of soil water content in a maize field using Electrical Resistivity Tomography. *Hydrology and Earth System Sciences*, **17**(2):595—609.
- Boaga, J., Rossi, M., and Cassiani, G. (2013). Monitoring Soil-plant Interactions in an Apple Orchard Using 3D Electrical Resistivity Tomography. *Procedia Environmental Sciences*, **19**:394—402.
- Burger, R., Sheehan, A.F. and Jones C.H. (2006). *Introduction to Applied Geophysics: Exploring the shallow subsurface*. W.W.Norton and Company.
- Cassiani, G., Boaga, J., Rossi, M., Putti, M., Fadda, G., Majone, B., and Bellin, A. (2016). Soil-plant interaction monitoring: Small scale example of an apple orchard in Trentino, North-Eastern Italy. *Science of the Total Environment*, **543**:851—861.
- Chambers, J. E., Gunn, D. A., Wilkinson, P. B., Meldrum, P. I., Haslam, E., Holyoake, S., Kirkham, M., Kuras, O., Merritt, A., and Wragg, J. (2014). 4D electrical resistivity tomography monitoring of soil moisture dynamics in an operational railway embankment. *Near Surface Geophysics*, **12**(1):61—72.
- Free, E. E. (1911). Studies in soil physics ii, the movements of soil water. *The Plant World*, **14**:59—66.
- Garré, S., Javaux, M., Vanderborght, J. Pagés, L., and Vereecken, H. (2011). Three dimensional electrical tomography to Monitor Root Zone Water Dynamics. *Vadose Zone Journal*, **10**(1):412—424.
- Lewis, J. and Sjostrom, J. (2010). Optimizing the experimental design of soil columns in saturated and unsaturated transport experiments. *Journal of Contaminant Hydrology*, **115**(1—4):1—13.
- Mooney, S. J., Pridmore, T. P., Helliwell, J., and Bennett, M. J. (2012). Developing X-ray computed

264 tomography to non-invasively image 3-D root systems architecture in soil. *Plant and Soil*, **352**(1—
265 2):1—22.

266 Mueller, L., Kay, B. D., Hu, C., Li, Y., Schindler, U., Behrendt, A., Shepherd, T. G., and Ball, B. C.
267 (2009). Visual assessment of soil structure: Evaluation of methodologies on sites in Canada, China and
268 Germany Part I: Comparing visual methods and linking them with soil physical data and grain yield of
269 cereals. *Soil and Tillage Research*, **103**(1):178—187.

270 Nyberg, L. (1996). Spatial variability of soil water content in the covered catchment at Gårdsjön, Sweden.
271 *Hydrological Processes*, **10**:89—103.

272 Paradelo, M., Katuwal, S., Moldrup, P., Norgaard, T., Herath, L., and de Jonge, L. W. (2016). X-ray CT-
273 Derived Soil Characteristics Explain Varying Air, Water, and Solute Transport Properties across a
274 Loamy Field. *Vadose Zone Journal*, **15**(4).

275 Peyton, R. L., Haeffner, B. A., Anderson, S. H., and Gantzer, C. J. (1992). Applying X-ray CT to measure
276 macropore diameters in undisturbed soil cores. *Geoderma*, **53**(3—4):329—340.

277 Samouëlian, A., Cousin, I., Tabbagh, A., Bruand, A., and Richard, G. (2005). Electrical resistivity
278 survey in soil science: A review. *Soil and Tillage Research*, **83**(2):173—193.

279 Shokri, N., Lehmann, P., Vontobel, P., and Or, D. (2008). Drying front and water content dynamics during
280 evaporation from sand delineated by neutron radiography. *Water Resources Research*, **44**(6):1—11.

281 Srayeddin, I. and Doussan, C. (2009). Estimation of the spatial variability of root water uptake of maize
282 and sorghum at the field scale by electrical resistivity tomography. *Plant and Soil*, **319**(1-2):185—207.

283 Tracy, S. R., Daly, K. R., Sturrock, C. J., Crout, N. M. J., Mooney, S. J., and Roose, T. (2015). Three-
284 dimensional quantification of soil hydraulic properties using X-ray Computed Tomography and image-
285 based modelling. *Water Resources Research*, **51**(2):1006—1022.

286 van Genuchten, M. and Pachepsky, Y. (2011). *Encyclopedia of Agrophysics*. Springer Netherlands.

287 Waxman, M. and Smits, L. (1968). Electrical conductivities in oil-bearing shaly sands. *Society of Petroleum*
288 *Engineers Journal*, **243**:107—122.

289 Wildenschild, D., Hopmans, J. W., Vaz, C. M. P., Rivers, M. L., and Rikard, D. (2002). Using X-ray
290 computed tomography in hydrology: systems , resolutions , and limitations. *Journal of Hydrology*,
291 **267**:285—297.

292

293

294

295

296

297

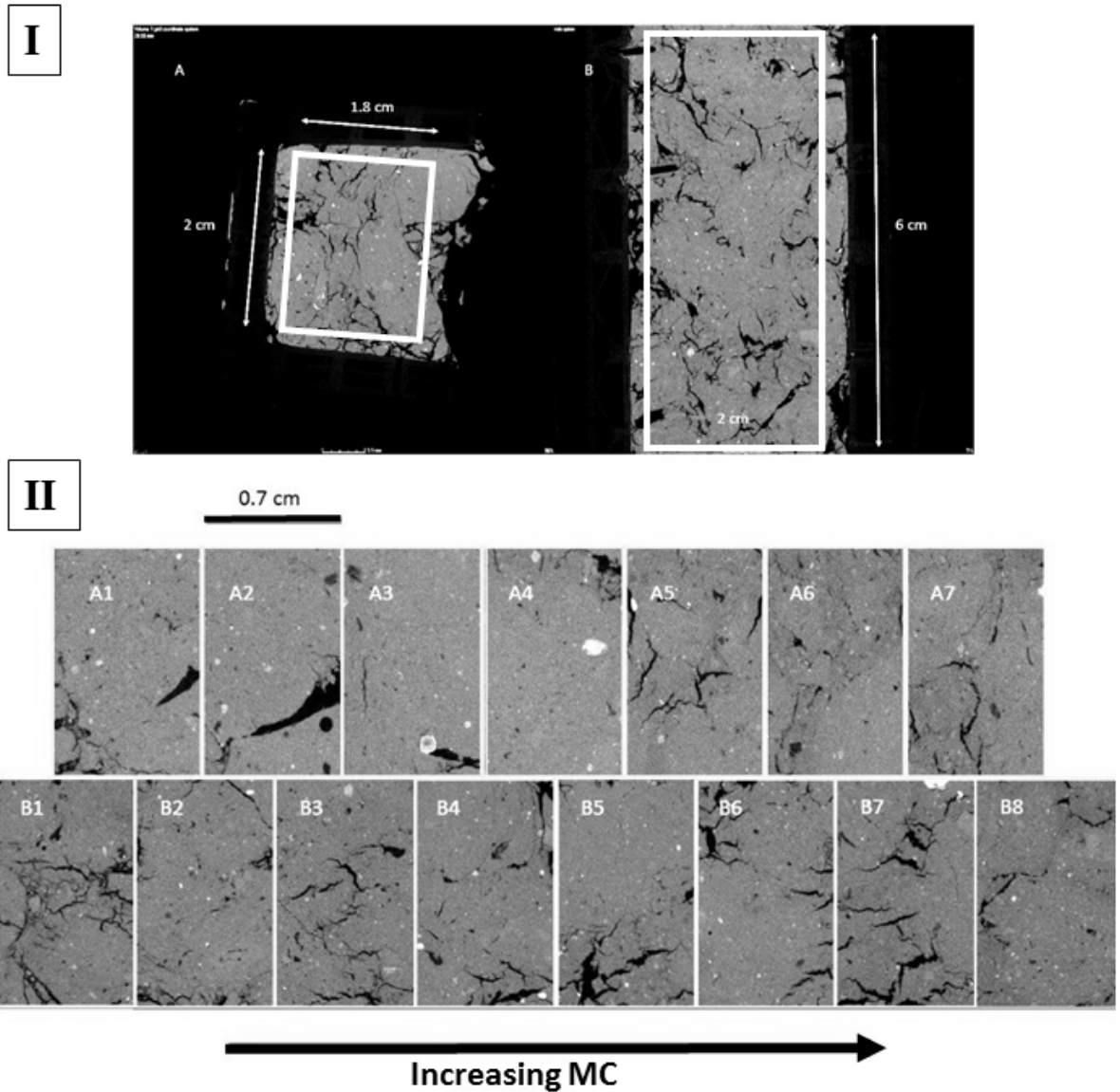
298

299

300

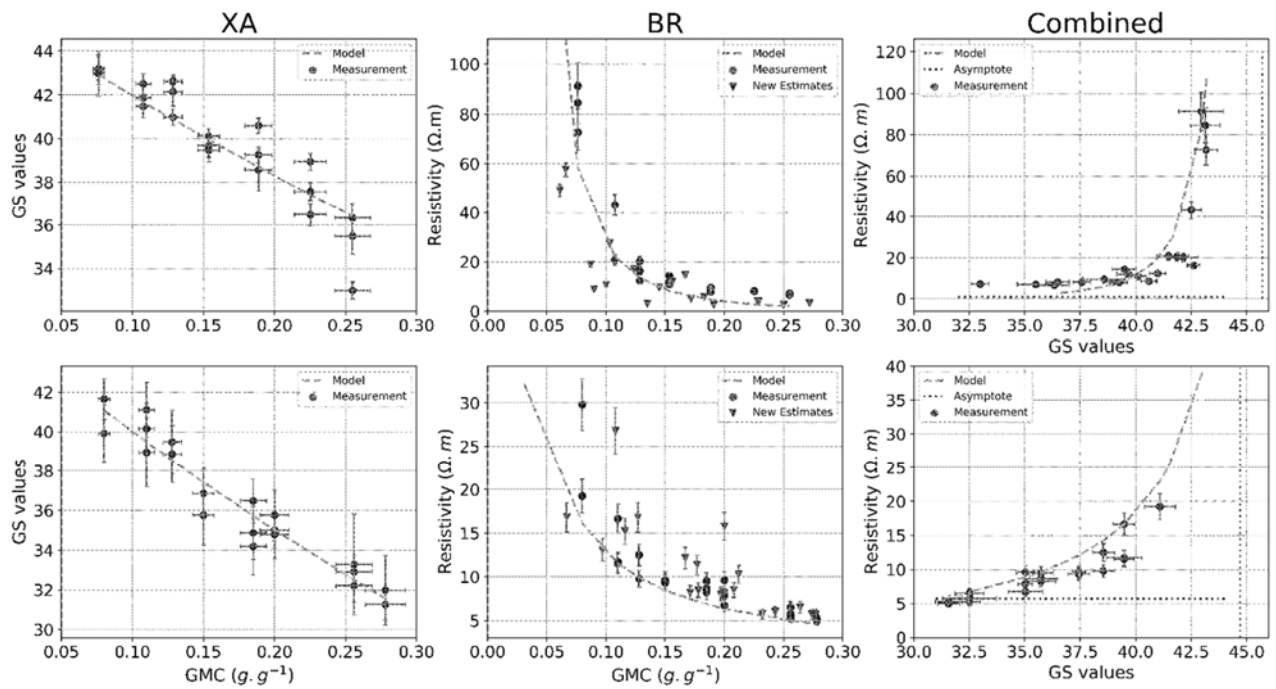
301

302
303



304
305
306
307
308
309
310
311
312
313
314
315
316

Figure 1. I: Image showing two cross-sections (I- Widthwise and B- Lengthwise) of a CT reconstructed soil volume. White rectangles indicate the selection area used for image processing. II: Selected area cropped from scan images corresponding to every soil batch. 'A' group corresponds to soil type 1 and 'B' group to soil type 2.



S1

S2

Figure 2. XA: Average GS measurements (circle) fitted by XA estimates (dashed line). Error bars indicate the GS standard deviation within the sample; BR: Resistivity measurements (circle) fitted by BR estimates based on laboratory measurements (dashed line) of MC and based on X-ray CT estimates (down triangle) of MC; Combined: Lab derived measurements fitted by the new pedophysical relation, Equation (5), estimates (dashed line). BR and Combined plots have an assumed 10% error for resistivity estimates.

		S1	S2
BR	ϕ (%)	35	30
	c (meq/100g)	27.2	37
	B_{ws} (S.cm ³ .m ⁻¹ .meq ⁻¹)	2	2
	m	2.84	0.87
	n	2.51	1.22
	D_g (g/cm ³)	2.65	2.65
	D_w (g/cm ³)	1	1
	σ_w (S/m)	0.05	0.05
BR lab fit	Pearson r	0.958	0.89
	RMSError	5.89	2.84
BR CT fit	Pearson r	0.97	0.93
	RMSError	4.43	2.22
XA	l_{dry} (GS)	46.04	42.5
	ρ_{dry} (kg/m ³)	4800	3794
	x_{dry} (m)	0.02	0.02
	μ_{water} (m ² /kg)	0.01186	0.01186
XA fit	Pearson r	0.93	0.96
	RMSError	1.1	1.9
Combined relationship fit	Pearson r	0.97	0.93
	RMSError	5.96	2.41

339

340

341

342

Table 1. Laboratory determined parameters used to compute BR and XA relationships and indicators describing the fit between measured data and model predictions.